JOURNAL OF GUIDANCE, CONTROL, AND DYNAMICS
Vol. 20, No. 3, May–June 1997

Comparison of Analytical Modeling of OEDIPUS Tethers with Data from Tether Laboratory

F. R. Vigneron,* A. M. Jablonski,† and R. Chandrashaker‡
Canadian Space Agency, St. Hubert, Quebec J3Y 8Y9, Canada
J. L. Bergmans§ and B. A. McClure¶
Carleton University, Ottawa, Ontario K1S 5B6, Canada
and
G. Tyc**
Bristol Aerospace Limited, Winnipeg, Manitoba R3C 2S4, Canada

The OEDIPUS missions employ suborbital rocket flights to study the space plasma of the ionosphere. An OEDIPUS payload comprises two spinning subpayloads that are connected by a tether that is up to 1000 m in length. Experiments that were undertaken with a Tether Laboratory Demonstration facility (TE-LAB) to confirm mathematical modeling of OEDIPUS are reported. A linear mathematical model of the dynamics of the ground-based configuration is outlined. The modeling entails the same methods that are used for the in-space OEDIPUS configuration and, in addition, includes effects important to the 1-*g* laboratory environment. An eigenvalue analysis of the model is presented that is based on damped gyroscopic natural modes. Stability criteria are obtained from analysis of positive definiteness of the stiffness matrix. Data from test cases obtained with the TE-LAB facility are presented. The data include experimental modal parameters obtained using a charge-coupled device camera and fast Fourier transform-based processing. The eigenvalues from the analytical model compare well over the parameter range investigated. The analytical stability criteria also match with TE-LAB results for end-body dynamics. However, modeling of nonlinearities would be required to explain some of the dynamics phenomena of the tether that are in evidence in the TE-LAB data.

Introduction

THE OEDIPUS type of configuration consists of two rocket subpayloads that each spin about their minor axes, payload-attached radial booms that are flexible and a connecting tether (Fig. 1). In the initial stages of the mission, the two subpayloads are connected and are deployed from the launch vehicle with a spin about their longitudinal axes. Booms are deployed, and then the subpayloads are separated by an impulse from a cold gas system. During separation, the tether deploys to a length of about 1 km, during which time its tension is held constant at about 1.1 N by the action of a magnetic hysteresis brake on its reel. After separation, the tether tension drops to a lower, near-zero value.

The mathematical modeling for the OEDIPUS flights is described in Refs. 1–5. In the first stage of modeling, emphasis was focused on understanding the behavior of a configuration with a single payload, a constant length tether (linear terms only), two sets of flexible booms, and nonlinear rotational dynamics of the payload. Nonlinearities of the tether have been explored for subcases.

The Tether Laboratory Demonstration System (TE-LAB) was developed to demonstrate the dynamics of the OEDIPUS type of configuration with physical hardware and to provide laboratory data for comparison with mathematical models.[6] TE-LAB is intended to be a ground-based scale model version of the mentioned first stage of OEDIPUS modeling. It is shown schematically in Fig. 2. However, it differs from the in-space configuration in the following ways: 1) it is much smaller due to laboratory ceiling height limitations, 2) the forces of gravity are greater in the laboratory than in the in-space environment, and 3) there are friction forces in supporting gimbals of the laboratory setup that are not present in space. In light of these differences, a separate mathematical model of TE-LAB was developed that incorporates the laboratory effects in addition to the in-flight phenomena. The same basic assumptions and methods were used for both the TE-LAB and the in-space model and, thus, validation of the TE-LAB mathematical model using experimental data contributes directly to validation of the in-flight model.

In the following, the relevant features of TE-LAB are first summarized. The linear mathematical model of TE-LAB is then described. The test program that was conducted with TE-LAB is outlined, and sample results are given. The test program concentrated on the dynamics of the rigid end body and its interaction with the tether. Experimental and theoretical results are compared, and agreements and shortcomings are summarized. Finally, the significance to the planned OEDIPUS-C flight is discussed.

TE-LAB and Measurement System

The main elements of TE-LAB are depicted schematically in Fig. 2 and include the following: 1) an end body supported by a 2-axis gimbal that is driven by a rotating table, 2) an upper rotating table with tether spool and tension application device (dc motor with hysteresis clutch), 3) a constant length of tether wire, and 4) a payload-orientation determination system. The tether is stranded tin-coated copper with Teflon® coating having a diameter of about 1 mm (Raychem 55a0111-24-9) and is the same wire as used in the OEDIPUS missions. The upper and lower drive motors are synchronized so that the tether does not twist during operation. The payload orientation determination system (PODS) has two reflective targets on top of the end body that are tracked with a charge-coupled device camera, and their positions in the field of view are used to compute three Euler angles that describe the attitude of the end body. A 486 PC computer system supports the control of the electric motors, the PODS operation, and data processing. The TE-LAB

Received Nov. 17, 1995; revision received Jan. 7, 1997; accepted for publication Jan. 10, 1997. Copyright © 1997 by F. R. Vigneron and A. M. Jablonski. Published by the American Institute of Aeronautics and Astronautics, Inc., with permission.

*Consultant, Space Technology Branch, 6767 route de l'aeroport. Senior Member AIAA.

†Research Scientist, Space Technology Branch, 6767 route de l'aeroport. Member AIAA.

‡Engineer, Space Technology Branch; currently Senior Engineer, Dynamics and Component Engineering, Pratt and Whitney Canada, Longueuil, Quebec J4G 1A1, Canada. Member AIAA.

§Graduate Student, Mechanical and Aerospace Engineering; currently Project Engineer, Special Projects Group, CFD Research Corporation, Huntsville, AL 35805. Member AIAA.

¶Graduate Student, Mechanical and Aerospace Engineering; currently Mechanical Engineer, Positioning Mechanisms, Hughes Space and Communications Company, El Segundo, CA 90245.

**Research Engineer, Rockets and Space Division. Member AIAA.

Table 1 Physical parameters of TE-LAB for various test configurations

Parameter	Symbol	Units	Major axis spinner, light tether	Minor axis spinner, light tether	Minor axis spinner, heavy tether
Tether					
Length to spool axis	ℓ	m	6.42	6.38	6.38
Mass/unit length	ρ	kg/m	0.003	0.003	0.0275
Tension range	T	N	0–5	0–5	0–5
Damping ($\%\Delta E/E$)			10	10	10
End body					
Spin inertia	C_0	kg-m^2	0.00625	0.00249	0.00249
Transverse inertia	A_0	kg-m^2	0.00542	0.00607	0.00607
Transverse inertia	B_0	kg-m^2	0.00538	0.00611	0.00611
Gimbal damping	$D_{g\psi}$	kg-m^2/s	0.00042	0.00042	0.00042
	$D_{g\theta}$	kg-m^2/s	0.00025	0.00025	0.00025
System					
Spin rate	S or ω_3	cps	0–3	0–3	0–3
Distance from end-body c.g. to tether connection	b	m	0.094	0.129	0.129

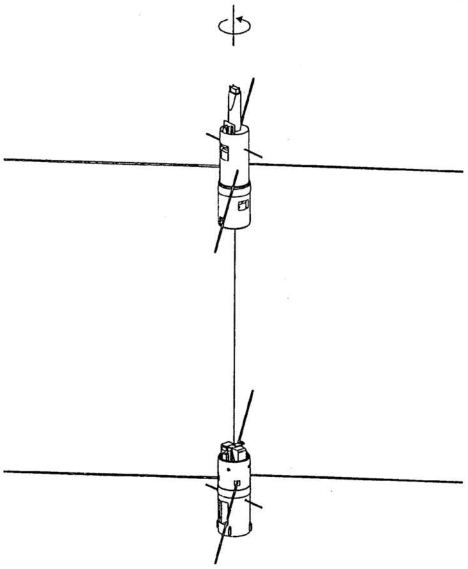

Fig. 1 **OEDIPUS configuration.**

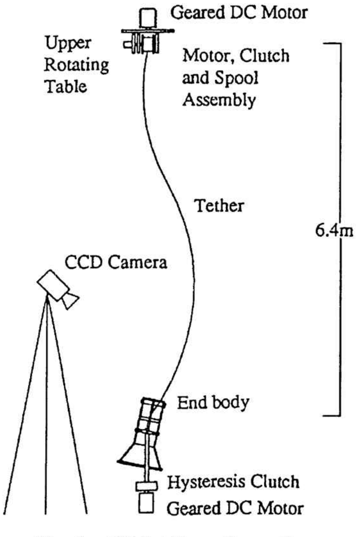

Fig. 2 **TE-LAB configuration.**

can be reconfigured easily to enable variations in payload inertia, tether length and type, and end-body attachment point. During operation, spin rate and tether tension can be varied or adjusted as desired within the limit of the equipment. The data acquisition system records tension (based on calibration of the spool's motor and clutch), spin rate, and camera image information that enables immediate calculation of time histories of the end-body attitude. The photograph of Fig. 3 shows the upper and lower table, an end body, and tether. The tether has lead weights added to create a heavy tether that extends the parameter range of tests. The TE-LAB is described fully in Refs. 6–8.

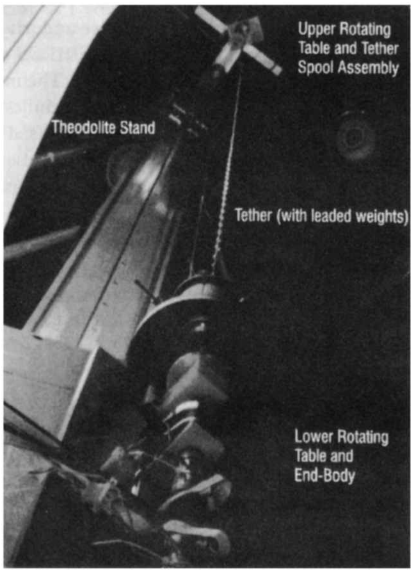

Fig. 3 **TE-LAB in the laboratory: major axis spinner, heavy tether.**

The nominal physical parameters that pertain to models of dynamic behavior of various test configurations described in later sections are summarized in Table 1. The light tether in Table 1 is the OEDIPUS tin-coated stranded copper wire. The heavy tether was fabricated by adding lead weights and was introduced to extend the range of parameters of the test program. The moments of inertia of the various end bodies were determined experimentally using a rocking pendulum type of measuring device.[7] The damping values of the support gimbals were also determined experimentally, by measuring the logarithmic decrement of test data of a gimbaled end body in pendulum type rocking motion.[7] The damping of the tether in the laboratory setup is due to air drag, to material hysteresis, and to the connection at the reel end. Damping was specified through an assumed modes model (outlined in the next section) with damping ratios of 10% energy loss per cycle.

Linear Mathematical Model of TE-LAB

The formulation of the linear mathematical model of TE-LAB is described fully in Ref. 9. The main steps are outlined herein to convey the method of analysis and the basic assumptions.

Differential Equations

Coordinates and variables of the end body and tether are shown in Figs. 4 and 5, respectively. The point 0 is fixed, and $[0X_1\ X_2\ X_3]$ is an inertial coordinate system. The upper end of the tether is constrained to be on $0X_3$ at $s = \ell$, where ℓ is the length of the tether.

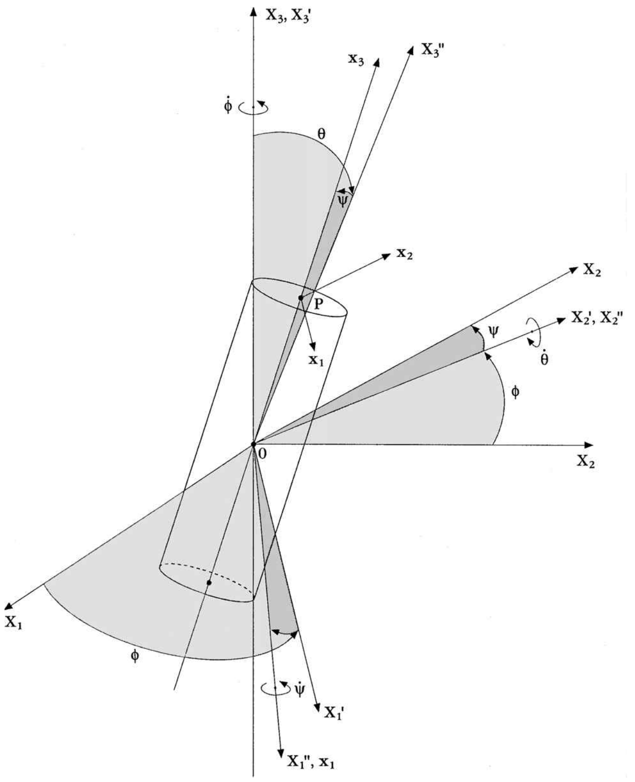

Fig. 4 Coordinates and variables of end body, 3–2–1 Euler angles sequence.

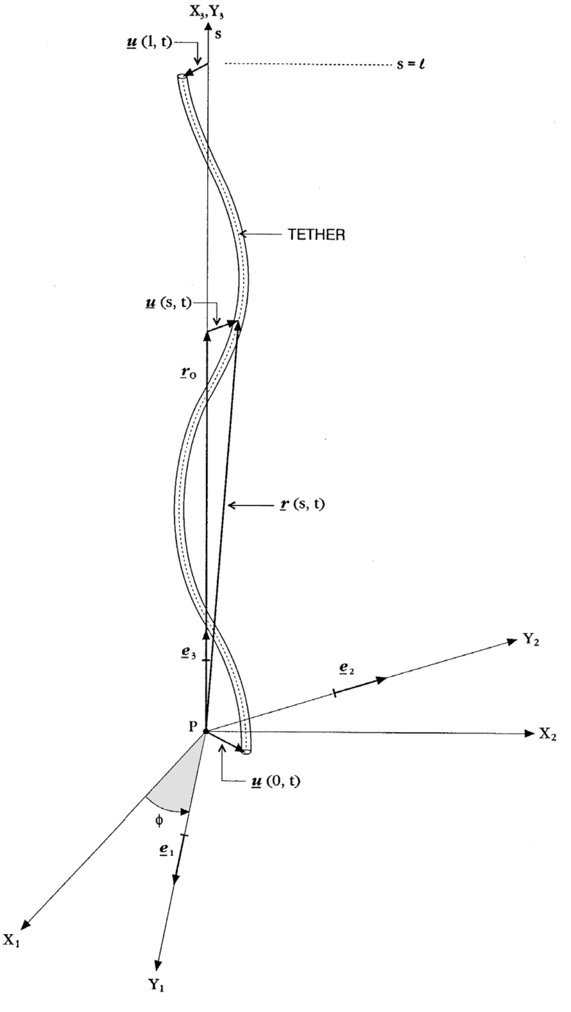

Fig. 5 Coordinates of the tether: $r(s,t) = r_0 + u(s,t)$ and $u(s,t) = u(s,t)e_1 + v(s,t)e_2 + w(s,t)e_3$.

The motion of the end body is defined by a 3–2–1 Euler angle rotational sequence. For small nutation, θ and ψ define the motion of the spin axis and χ defines the spin angle. The kinetic energy of the end body is

$$T_B = \tfrac{1}{2}A_0\omega_1^2 + \tfrac{1}{2}B_0\omega_2^2 + \tfrac{1}{2}C_0\omega_3^2 \tag{1}$$

where A_0, B_0, and C_0 are moments of inertia and ω_1, ω_2, and ω_3 are angular rates of the end body. The angular rates are functions of the Euler angles, and to linear order they are

$$\omega_1 = \dot{\psi} - \dot{\chi}\theta \qquad \omega_2 = \dot{\theta} + \dot{\chi}\psi \qquad \omega_3 = \dot{\chi} \tag{2}$$

The deformation of the tether is defined relative to $[PY_1 \; Y_2 \; Y_3]$ (Fig. 5), which rotates with the spin angle of the lower end body. The displacement has components $u(s,t)$, $v(s,t)$, and $w(s,t)$. The end body and tether are connected at point P and, hence, the Euler angles and tether coordinates are interrelated as follows:

$$u(0,t) = b\theta \qquad v(0,t) = -b\psi \qquad w(0,t) = -\tfrac{1}{2}b(\psi^2 + \theta^2) \tag{3}$$

The kinetic energy of the tether has the following form:

$$T_t = \frac{1}{2}\int_0^{\ell}(\dot{u}^2 + \dot{v}^2 + \dot{w}^2)\rho\,\mathrm{d}s + \omega_3\int_0^{\ell}(u\dot{v} - \dot{u}v)\rho\,\mathrm{d}s + \omega_3^2\int_0^{\ell}(u^2 + v^2)\rho\,\mathrm{d}s \tag{4}$$

In the preceding expression, ρ is the mass of the tether per unit length.

The work due to the tension applied to the tether at $s = \ell$ may be shown to be

$$W_t = -\frac{1}{2}T\int_0^{\ell}\left(u_s^2 + v_s^2\right)\mathrm{d}s - \frac{1}{2}Tb(\theta^2 + \psi^2) \tag{5}$$

The work associated with the Earth's gravity field has the form

$$W_g = \frac{1}{2}\rho g\ell b(\theta^2 + \psi^2) + \frac{1}{2}\int_0^{\ell}\rho g(\ell - s)\left(u_s^2 + v_s^2\right)\mathrm{d}s \tag{6}$$

where T is tether tension, g is the gravitational constant, the subscript s denotes differentiation with respect to s, and b is the distance from 0 to the attachment point of the tether.

The tether deformations are discretized with assumed shape factors. The series that take into account the appropriate natural boundary conditions follows:

$$\begin{aligned} u(s,t) &= (1 - \xi)b\theta(t) + \ell\Phi^T(\xi)q_u(t) \\ v(s,t) &= -(1 - \xi)b\psi(t) + \ell\Phi^T(\xi)q_v(t) \end{aligned} \tag{7}$$

where $\xi = s/\ell$, Φ is a column matrix of n assumed sinusoidal shape functions, $q_u(t)$ and $q_v(t)$ are column matrices of corresponding time-dependent tether deformation variables, and

$$\Phi(\xi) = \begin{bmatrix} \sin\pi\xi \\ \bullet \\ \bullet \\ \sin n\pi\xi \end{bmatrix} \qquad q_u(t) = \begin{bmatrix} q_{u1}(t) \\ \bullet \\ \bullet \\ q_{un}(t) \end{bmatrix} \qquad q_v(t) = \begin{bmatrix} q_{v1}(t) \\ \bullet \\ \bullet \\ q_{vn}(t) \end{bmatrix} \tag{8}$$

Substitution of Eqs. (7) into Eqs. (4–6) results in expressions for the potentials T_t and W_t in terms of the discrete variables. Lagrange's equations can then be applied with the potentials to obtain the motion equations. Linearization of the spin variable $\omega_3(t)$ follows about a constant spin rate S. The motion equations are obtained, after lengthy but straightforward algebra, in the second-order form

$$\boldsymbol{M}\ddot{\boldsymbol{x}} + (\boldsymbol{D} + \boldsymbol{G})\dot{\boldsymbol{x}} + \boldsymbol{K}\boldsymbol{x} = \boldsymbol{0} \tag{9}$$

The state variable in Eq. (9) is $\boldsymbol{x}^T = [\psi, \theta, q_u^T, q_v^T]$. The matrix coefficients are constant and are

$$\boldsymbol{M} = \begin{bmatrix} A & 0 & 0 & -R^T \\ 0 & B & R^T & 0 \\ 0 & R & M & 0 \\ -R & 0 & 0 & M \end{bmatrix} \qquad \boldsymbol{D} = \begin{bmatrix} D_{g\psi} & 0 & 0 & 0 \\ 0 & D_{g\theta} & 0 & 0 \\ 0 & 0 & C_t & 0 \\ 0 & 0 & 0 & C_t \end{bmatrix}$$

$$\boldsymbol{G} = \begin{bmatrix} 0 & -(A+B-C)S & -2SR^T & 0 \\ (A+B-C)S & 0 & 0 & -2SR^T \\ 2SR & 0 & 0 & -2SM \\ 0 & 2SR & 2SM & 0 \end{bmatrix}$$

$$\boldsymbol{K} = \begin{bmatrix} (C-B)S^2 + (T_t - T_g)b & 0 & 0 & S^2R^T - Q_g^T \\ 0 & (C-A)S^2 + (T_t - T_g)b & -\left(S^2R^T - Q_g^T\right) & 0 \\ 0 & -(S^2R - Q_g) & K_T - K_g - S^2M & 0 \\ S^2R - Q_g & 0 & 0 & K_T - K_g - S^2M \end{bmatrix}$$

The coefficients within the matrices are defined as

$$A = A_0 + \tfrac{1}{3}\rho\ell b^2 \qquad B = B_0 + \tfrac{1}{3}\rho\ell b^2 \qquad C = C_0$$

$$T_t = T[1 + (b/\ell)] \qquad T_g = \rho g\ell[1 + (b/2\ell)]$$

$$R = \rho\ell^2 b \int_0^1 (1-\xi)\Phi \,\mathrm{d}\xi \qquad M = \rho\ell^3 \int_0^1 \Phi\Phi^T \,\mathrm{d}\xi$$

$$Q_g = \rho g\ell b \int_0^1 (1-\xi)\Phi_\xi \,\mathrm{d}\xi$$

$$K_t = T\ell \int_0^1 \Phi_\xi \Phi_\xi^T \,\mathrm{d}\xi \qquad K_g = \rho g\ell^2 \int_0^1 (1-\xi^2)\Phi_\xi \Phi_\xi^T \,\mathrm{d}\xi$$

C_t is the coefficient of a linear viscous damping term that is added to represent material damping of the tether. $D_{g\psi}$ and $D_{g\theta}$ are coefficients of linear viscous gimbal damping terms. The subscript ξ refers to differentiation. The mass, damping, and stiffness matrices, $\boldsymbol{M}, \boldsymbol{D}$, and $\boldsymbol{K}$, respectively, are symmetric. The gyroscopic matrix $\boldsymbol{G}$ is skew symmetric. The equations define a linear, vibratory, damped, gyroscopic system.

Eigenproblem Analysis

The damped gyroscopic modes and frequencies may be derived from Eq. (9) using methods of Ref. 10. Equation (9) may be rearranged to the following form:

$$\boldsymbol{A}\dot{\boldsymbol{Z}} + \boldsymbol{B}\boldsymbol{Z} = \boldsymbol{0} \tag{10}$$

where

$$\boldsymbol{Z} = \begin{bmatrix} \dot{\boldsymbol{x}} \\ \boldsymbol{x} \end{bmatrix} \qquad \boldsymbol{A} = \begin{bmatrix} \boldsymbol{M} & \boldsymbol{0} \\ \boldsymbol{0} & \boldsymbol{K} \end{bmatrix} \qquad \boldsymbol{B} = \begin{bmatrix} \boldsymbol{D} & \boldsymbol{0} \\ \boldsymbol{0} & \boldsymbol{0} \end{bmatrix} + \begin{bmatrix} \boldsymbol{G} & \boldsymbol{K} \\ -\boldsymbol{K} & \boldsymbol{0} \end{bmatrix}$$

$\boldsymbol{A}$ is symmetric and positive definite and has dimension $4n + 4$. $\boldsymbol{B}$ is the sum of a skew symmetric and a symmetric part and has dimension $4n + 4$. For this structure of equation, the eigenproblem has $4n + 4$ eigenvalues that are in conjugate pairs,

$$\lambda_k = -\sigma_k + i\nu_k \qquad \lambda_k^* = -\sigma_k - i\nu_k \tag{11}$$

The σ_k and ν_k convert to natural modal frequencies and modal damping ratios by the formula

$$\omega_k^2 = \nu_k^2 + \sigma_k^2 \qquad \varsigma_k = \sigma_k \Big/ \sqrt{\nu_k^2 + \sigma_k^2} \tag{12}$$

The $4n + 4$ corresponding eigenvectors have the form

$$\boldsymbol{Z}_k = \begin{bmatrix} \lambda_k(\boldsymbol{U}_k + i\boldsymbol{V}_k) \\ \boldsymbol{U}_k + i\boldsymbol{V}_k \end{bmatrix} \tag{13}$$

where $\boldsymbol{U}_k$ and $\boldsymbol{V}_k$ are real-valued parts of a complex eigenvector. The damped gyroscopic mode shape has the following form:

$$\boldsymbol{x}_k = e^{-\sigma_k t}\{\boldsymbol{U}_k \cos\nu_k t - \boldsymbol{V}_k \sin\nu_k t\} \tag{14}$$

where $\boldsymbol{x}_k(t)$ is the kth mode shape expressed in terms of real-valued quantities.

A typical graph of modal frequencies and modal damping ratios vs spin rate is shown in Fig. 6. Examples of corresponding mode shapes are shown in Fig. 7. The modes group into categories: 1) tether modes, which are dependent on tether mass and tension and to a much lesser extent on the end body (e.g., all modes except $f = 3.151$ Hz in Fig. 7), and 2) one end-body nutation mode, which is predominantly dependent on end-body inertias and tether tension and to a much lesser extent on tether mass (e.g., $f = 3.151$ Hz in Fig. 7); there is also a spin mode, which has frequency S if the spin rate is sufficiently high and/or the tether coupling is weak.

In addition, the following characteristics have been noted through computer analyses, and they are evident in Fig. 6. Graphs that illustrate the points more fully are presented in Ref. 7.

1) When the configuration is not spinning (i.e., $S = 0$), the frequencies are double roots of the eigenvalue problem; this is consistent with the symmetry about the transverse axes of the end body and the tether.

2) When the configuration is spinning at low speed (i.e., S is less than about 0.5 Hz), the frequencies and damping ratios are positive, which indicates stability of the equilibrium state.

3) There are critical values of S where a particular frequency is zero; the corresponding damping ratio is noted to change sign at these values. Below the critical value of S, the stabilizing effect of tether tension dominates the destabilizing effect of tether centrifugal force; above the critical value, the reverse is true and the corresponding tether mode is unstable.

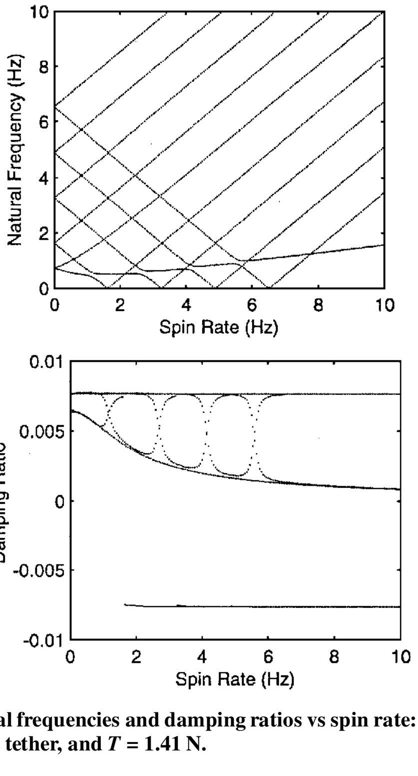

Fig. 6 Modal frequencies and damping ratios vs spin rate: major axis spinner, light tether, and T = 1.41 N.

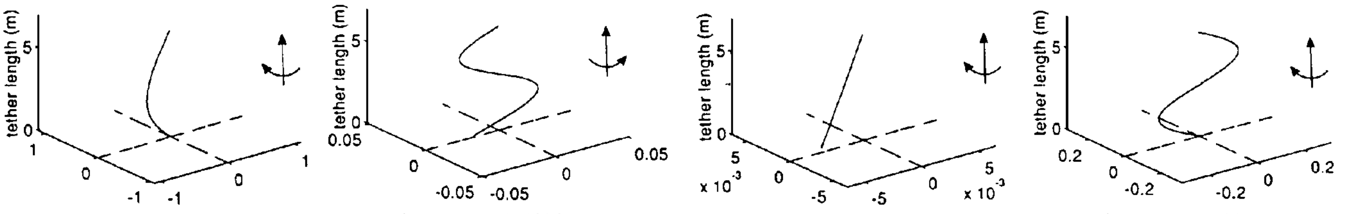

Natural frequency: 1.356 **Natural frequency: 0.6414** **Natural frequency: 3.151** **Natural frequency: 6.296**

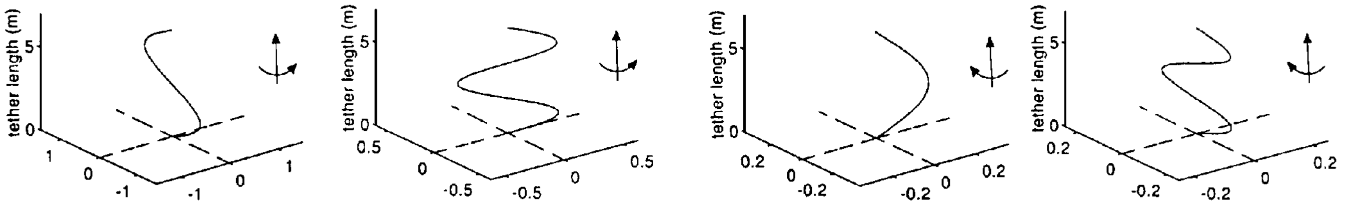

Natural frequency: 0.2724 **Natural frequency: 1.949** **Natural frequency: 4.65** **Natural frequency: 7.944**

Fig. 7 Damped gyroscopic mode shapes: major axis spinner, light tether, $T = 1.41$ N, and $S = 3.0$ Hz.

4) For the major axis spinner configurations of the TE-LAB, the nutation mode is stable (i.e., the nutation frequency is nonzero for all values of S). For minor axis spinner configurations, the nutation mode may be stable or unstable, depending on tension, spin rate, and other parameters.

Stability Criteria

The state variables of Eq. (9) are coupled by the tether damping. Hence, the system is stable if and only if the $\boldsymbol{K}$ matrix is positive definite.[3,11] This condition has been reduced by Tyc[3] for the case with three assumed tether shapes. Two sets of criteria for stability are obtained.

1) Tether-associated criteria

$$T \geq \frac{\rho \ell^2 S^2}{n^2 \pi^2} + \frac{\rho g \ell}{2} - \frac{2 \rho g^2 \ell^3 \Omega^g_{n-1,\,n}}{n^2 \pi^2 \lambda_n} \qquad n = 1, 2, \ldots \tag{15}$$

2) End-body (payload)-associated criterion

$$C_0 - A_0 \geq \frac{1}{3} \rho \ell b^2 + \frac{1}{S^2} \sum_{n=1}^{n=3} \frac{k_n^2}{\lambda_n} - \frac{bT}{S^2}\left(1 + \frac{b}{\ell}\right) + \frac{\rho g \ell b}{S^2}\left(1 + \frac{b}{2\ell}\right) \tag{16}$$

The constants k_n, λ_n, and $\Omega^g_{n,\,m}$ are recursive and are defined fully in Ref. 8. The criteria do not depend on gimbal or tether damping, as they are derived solely from the $\boldsymbol{K}$ matrix. Relation (16) is the well-known maximum-moment-of-inertia criterion for stability of the gyroscopic end body, with extensions to include the stabilizing effect of tether tension and the destabilizing effect of tether spin. Also the effect of laboratory gravity is included.

These stability criteria are presented in graphical form in Fig. 8 for a TE-LAB parameter set that comprises a minor axis spinner and a light tether. The dotted lines in the tension vs spin rate graph are locations where the left-hand side equals the right-hand side in relations (15) and (16). To the left of line labeled P, the criterion of relation (16) is satisfied. To the left of T1, T2, and T3, the criteria of relation (15) are satisfied for $n = 1$, 2, and 3, respectively. Thus, in theory the TE-LAB motion is forecast to be unstable where its (T, S) coordinate on the graph is in the shaded region. Configurations below the minimum tension line are physically unrealizable in the laboratory (the force of gravity on the tether exceeds the suspending tension). The relative locations of the P and T1, T2, and T3 lines turn out to be different for various combinations of TE-LAB parameters. The combinations will be illustrated in the section on comparison of experiment and theory.

The stability boundaries can also be obtained from analysis of where the natural frequencies are zero.[7] The gravity force in the laboratory influences the location of the stability boundaries to some extent,[7] as is illustrated in Fig. 9.

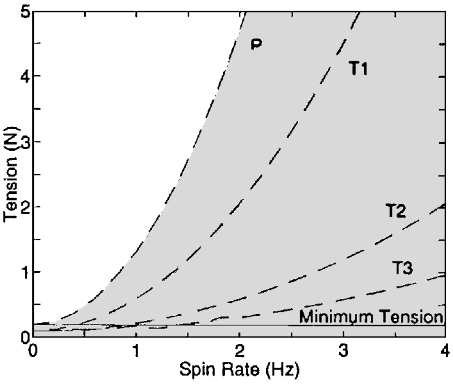

Fig. 8 Stability criteria: minor axis spinner, light tether.

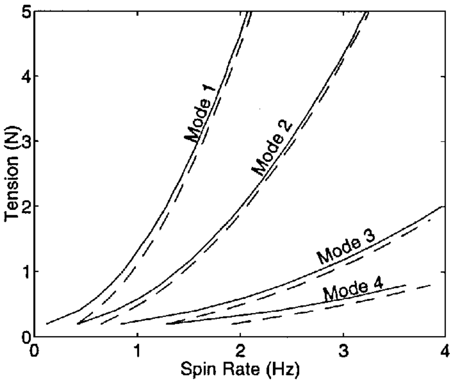

Fig. 9 Effect of gravity on stability boundaries: minor axis spinner, heavy tether; ——, with gravity and - - -, without gravity.

TE-LAB Results and Comparison with Modeling

Test Program and Procedures

Tests were grouped into three categories: minor axis spinner with light tether, minor axis spinner with heavy tether, and major axis spinner with light tether. The physical parameters of the corresponding configurations are in Table 1. Spin rates and tensions for each configuration are summarized in Table 2.

For end bodies that appeared stable, two types of initial conditions were imparted experimentally. The first was a torque-free kick applied by hand to the end body. The second was a tether pluck, where the tether was pulled by hand several inches from the spin axis and released. Configurations that tended to be unstable were subjected to a third initial condition, namely, zero angle, zero tether deformation; in this case the end body was stabilized by hand about the vertical and released. To verify the repeatability of the tests, the minor axis spinner with light tether was tested twice.

Table 2 Summary of tests of spinning end body and tether

Spinner type	Tether type	Tether tension, N	Spin rate, Hz (for each tension)	No. of times tested
Minor axis	light	0.5, 0.89, 1.42, 2.76, 2.54	0, 0.5, 0.75, 1.0, 1.25, 1.5, 2.0, 2.25, 2.5, 2.75, 3.0	2
Minor axis	heavy	2.02, 3.51, 4.54	0, 0.5, 0.75, 1.0, 1.5, 2.0, 2.5, 3.0	1
Major axis	light	0.49, 1.41, 4.54	0, 0.5, 0.75, 1.0, 1.5, 2.0, 2.5, 3.0	1

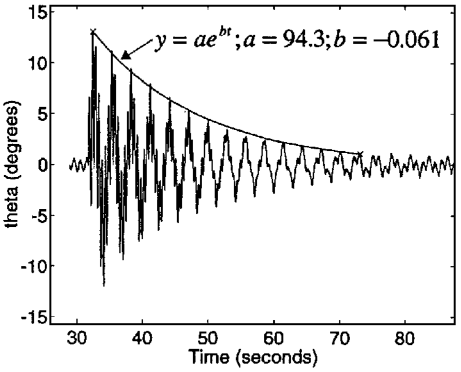

Fig. 10 Sample run A: minor axis spinner, light tether, *T* = 2.76 N, and *S* = 1 Hz.

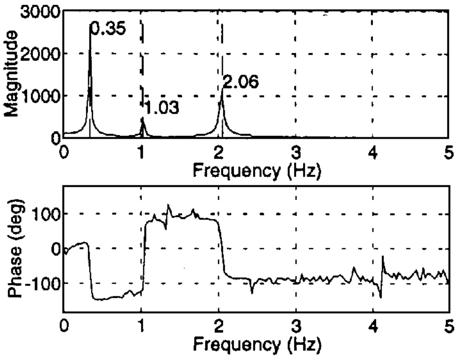

Fig. 11 FFT of sample run A.

Experiment Observations of End-Body Angular Motions

Sample run A (Fig. 10) is a typical case where the angular motion of the end body converges in the direction of the $\boldsymbol{x} = \boldsymbol{0}$ equilibrium state from a nonzero initial condition. It is a minor axis spinner with light tether, at a tension of 2.76 N and spin rate of 1 Hz. The TE-LAB measurement system is able to detect changes in angle of less than 0.1 deg, and its absolute accuracy is $+/-0.5$ deg or better for end-body angles of 12 deg or less.[8] In reality convergence to zero is never perfectly achieved with TE-LAB, due to mechanical imbalance and other imperfections. The minimum angle attained after convergence (θ or ψ or nutation) was about 1 deg. An exponential curve fit for this response is also shown in Fig. 10; the coefficient b (of e^{bt}) works out to -0.061 and gives a measure of the convergence rate of the time history. The tether deformations appeared random but bounded during visual observation. A fast Fourier transform (FFT) of data, presented in Fig. 11, shows that the attitude motion comprises the superposition of three harmonic modes of frequencies 0.35, 1.03, and 2.06 Hz.

Sample run B (Fig. 12) illustrates divergent behavior. It is from the same series of tests as sample run A, but with a higher spin rate (1.75 Hz). The coefficient b works out to $+0.020$ for these data, which gives a measure of the divergence rate. The observed tether motion was random but bounded. FFTs of this category of motion were also obtained, to identify the spectral content of both converging and diverging modes.[7,8]

Sample run C (Fig. 13) illustrates a case where θ and ψ diverge from the $\boldsymbol{x} = \boldsymbol{0}$ equilibrium state but converge to a limit cycle. The nutation angle of the limit cycle, which is given approximately by $\nu^2 = \theta^2 + \psi^2$, is about 25 deg. The configuration is a minor axis spinner with a light tether, with spin rate of 0.5 Hz and tension of 0.5 N. The tether motion was small and not resonant. The exponent b associated with the divergent part of this motion was $+0.503$, which was very high.

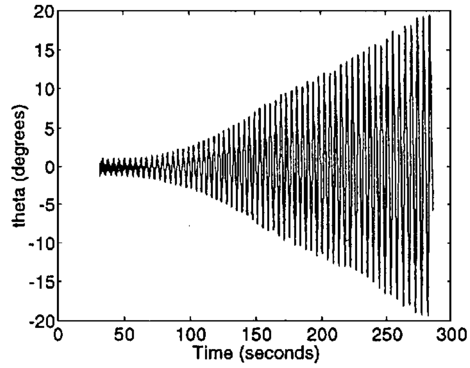

Fig. 12 Sample run B: major axis spinner, light tether, *T* = 2.76 N, and *S* = 1.75 N.

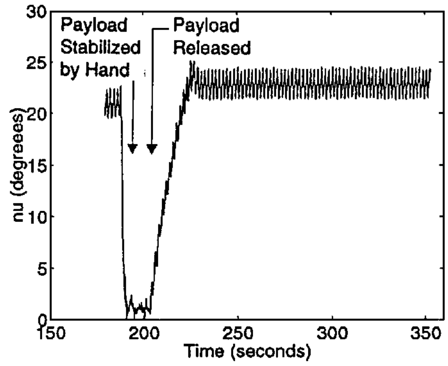

Fig. 13 Sample run C: minor axis spinner, light tether, *T* = 0.5 N, and *S* = 0.5 Hz.

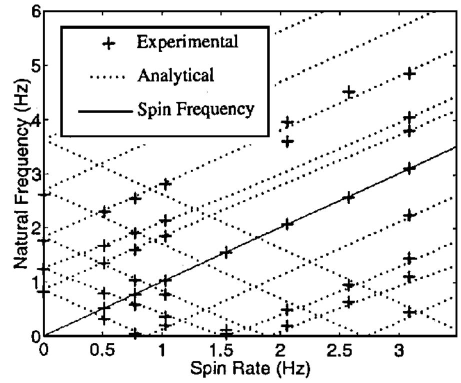

Fig. 14 Comparison of modal frequencies: minor axis spinner, heavy tether, and *T* = 4.54 N.

Comparison of Measured and Theoretical Natural Modal Frequencies

Figure 14 is a sample of the comparison between measured and calculated frequencies of the system modes. The configuration is a minor axis spinner with a heavy tether and tension of 4.54 N. Six assumed shapes were used for discretization of the tether in the analytical calculation. The measured frequencies were obtained from FFT processing of an end-body Euler angle, as is illustrated in Fig. 11. The resolution of the FFTs was between 0.02 and 0.12, depending on the number of samples chosen for processing. The numerical values of the FFT frequencies were generally repeatable to within 2–3% from one test to another. The experiment results are observed to be in excellent agreement with the analytical calculations, for both converging and diverging cases. A frequency corresponding to the TE-LAB spin rate appears in the data; this frequency is not forecast by the mathematical model but is rationalized to be due to

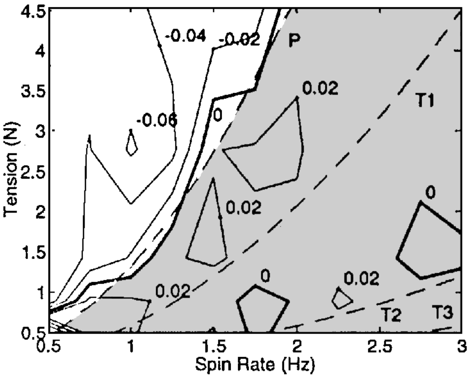

Fig. 15 Contours of constant *b* superimposed on theoretical stability graph: minor axis spinner, light tether; bold line is experimental stability boundary.

imbalance of the rotating end body and/or to an unmodeled small inner gimbal ring in the end body. In some cases there is a seeming absence of an experiment point to confirm an analytical calculation, e.g., at $S = 2.6$ Hz; it is very possible that such modes were simply missed experimentally because of a response below the threshold of measurement.

Reference 7 presents results for other configurations. In all cases agreement is excellent, thus validating the natural frequency calculation of the linear mathematical model.

Comparison of Measured Convergence/Divergence Boundaries with Theoretical Stability Criteria

The measured exponential time coefficients b (described earlier) have been organized into constant-value contours in the tension-spin rate format illustrated in Fig. 8. For each system configuration, a surface was interpolated from the b of all tests in the tension-spin rate plane. The numerical computation software MATLAB® was used to perform this interpolation and to generate contour curves of constant b. An experiment-derived contour with $b = 0$, thus, is the counterpart of the theoretical stability boundary (Fig. 8) and criteria (15) or (16). There are three categories of this type of stability graph, in accordance with the relative positioning of the P and T lines of the theoretical calculation shown in Fig. 8.

Figure 15 shows the first of the three categories. The configuration is a minor axis spinner with a light tether. The contours in this figure were generated based on the interpolation of 55 tests performed in this tension-spin rate plane. The underlying dotted lines and shaded areas are from the theoretical calculation. The lowest natural frequency is the end-body nutational mode, and the tether modes have higher frequencies; thus, the P line lies to the left of the T1–T3 lines. The solid lines are the contours constructed from the experiment-derived values of the exponential coefficient b. The comparison reveals the following.

1) The $b = 0$ contour matches reasonably well with the P line and, thus, the theoretical end-body (payload) criterion (16) agrees with experiment.

2) To the left of the P line, experiment and theory both indicate convergence and stability.

3) To the right of the P line, experiment and theory generally both indicate divergence/instability with the exception of the two small areas that are encircled by zero contours.

4) The two experiment-derived zero contours that encircle convergent areas in the shaded region are not within the scope of the linear model. Tests in these areas were found to have negative exponential time constants. It is conjectured that the model does not include them because of missing nonlinear terms in the tether dynamics. The regions may represent small nonzero limit cycles that are below the resolution of the TE-LAB/PODS setup.

Figure 16 shows the second category of stability graph, in which theoretical calculations indicate that the P line lies to the right of a T1 line. The data correspond to a minor axis spinner with a heavy tether. The lowest frequency is a tether mode, and the end-body nutation mode is the second lowest. Of most significance is that the experimental $b = 0$ stability contour matches the P line and not the T1 line as would be expected from the linear theory. Thus, experiment validates relation (16) as the correct practical indicator of stability and not relation (15). It is conjectured that this shortcoming in the modeling is also associated with the lack of nonlinear terms in the tether dynamics.

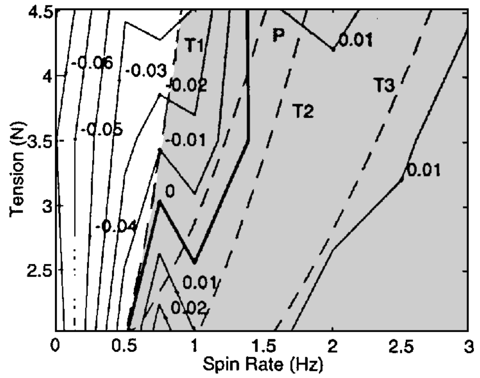

Fig. 16 Contours of constant *b*: minor axis spinner, heavy tether.

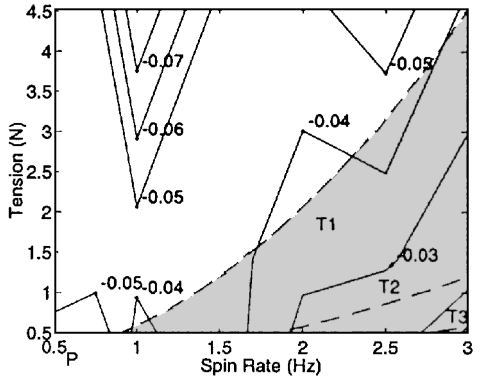

Fig. 17 Contours of constant *b*: major axis spinner, light tether.

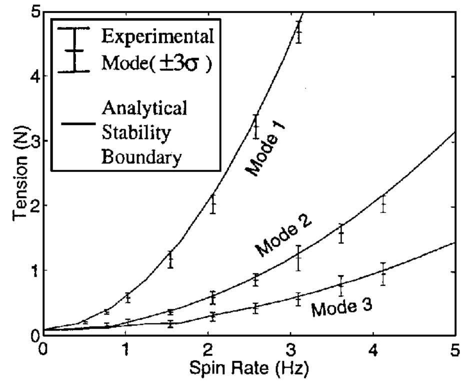

Fig. 18 Occurrences of tether resonances as a function of tension and spin rate: minor axis spinner, light tether.

Figure 17 illustrates the third category of stability graph, which is characterized by the absence of a P line. The figure corresponds to a major axis spinner with a light tether. The theoretical calculation of the nutation mode always turns out stable and, thus, Fig. 17 has no P line. According to theory, the system should be unstable to the left of the T1 line; however, the experimental data clearly exhibit stability.

Visual Observation of Tether Resonance

Tests were done where the spin rate was held constant and the tension was very slowly lowered from a high value to nearly zero. At certain values of tension, the tether motion developed into various pure vibratory modes with significant but bounded amplitude. Figure 18 shows the data from such tests. The experimental resonance lines coincide with the tether-related stability boundaries (i.e., lines T1–T3 of Fig. 15), which were obtained from relation (15).

Thus, in practice relation (15) identifies the conditions for which pure mode shapes of bounded amplitude will appear rather than instabilities as forecast by the linear mathematical model.

Summary Regarding Experiment vs Theory

The comparisons of Figs. 14–18 lead to the following general conclusions.

1) The linear model forecasts the damped gyroscopic natural modal frequencies very well, for both converging and diverging modes. The accuracy forecasting model frequencies is within about 5% for the significant modes.

2) The end-body (payload) stability criterion (16) is validated by measurements over a substantial range of parameter combinations. As an illustration of accuracy, the calculated critical spin rates are typically within about 15% of those measured in the tests.

3) The tether-mode instabilities that the mathematical model indicates via relation (15) do not appear as fully divergent instabilities in laboratory measurements. In the laboratory, the forecast instabilities turn out to be observed as pure tether modes of substantial but bounded amplitude and they occur only near the calculated stability boundaries.

4) The following phenomena are not within the scope of the linear mathematical model and are likely associated with missing nonlinearities in the tether modeling: nonzero limit cycles, e.g., Fig. 13, small regions of stability where instability is expected, e.g., Fig. 15, and point 3.

The results of this study contributed immensely to the confident understanding of tether and end-body dynamics prior to the launch of OEDIPUS-C in November 1995 (Ref. 12).

Concluding Remarks

This work demonstrates the strengths and shortcoming of the mathematical modeling being used for the OEDIPUS missions. The experimental results show that the theoretical models of the most important characteristics, namely, modal frequencies and payload attitude stability, can be used with confidence. Linear modeling does not fully describe all of the observed dynamics phenomena, however; for some parameter sets it may forecast a tether mode instability that is at most a bounded tether resonance, and it may overlook certain regions of convergent attitude motion and limit cycle behavior.

References

[1] Tyc, G., and Han, R. P. S., "Attitude Dynamics Investigation of the OEDIPUS-A Tethered Rocket Payload," *Journal of Spacecraft and Rockets*, Vol. 32, No. 1, 1995, pp. 133–141.

[2] Tyc, G., Vigneron, F. R., and Jablonski, A. M., "Tether Dynamics Investigations for the Canadian OEDIPUS and BICEPS Missions," International Round Table on Tethers in Space, European Space Agency/European Space Research and Technology Center, ESA WPP-081, Noordwijk, The Netherlands, Sept. 1994.

[3] Tyc, G., Han, R. P. S., Vigneron, F. R., Jablonski, A. M., Modi, V. J., and Misra, A. K., "Dynamics and Stability of a Spinning Tethered Spacecraft with Spinning Flexible Appendages," *Advances in the Astronautical Sciences 1993*, Vol. 85, Univelt, San Diego, CA, 1994, pp. 877–896 (AAS 93-736).

[4] Han, R. P. S., "Resonant Conditions for a Stretched Spinning Tether," *4th International Conference on Tethers in Space* (Washington, DC), Science and Technology Corp., Hampton, VA, 1995, pp. 1325–1340.

[5] Misra, A. K., "Dynamics of Low-Tension Spinning Tethers," *4th International Conference on Tethers in Space* (Washington, DC), Science and Technology Corp., Hampton, VA, 1995, pp. 1309–1324.

[6] Jablonski, A. M., Vigneron, F. R., Chandrashaker, R., Bergmans, J. L., McClure, B., Staley, D. A., and Tyc, G., "Tether Laboratory Demonstration System (TE-LAB)—A Ground Test Facility For The OEDIPUS Tether Missions," *4th International Conference on Tethers in Space* (Washington, DC), Science and Technology Corp., Hampton, VA, 1995, pp. 1809–1822.

[7] McClure, B. A., "The Tether Laboratory Demonstration System (TE-LAB)—Design, Operation, and Mathematical Model Validation Using an Eigenvalue Approach," M.S. Thesis, Mechanical and Aerospace Engineering Dept., Carleton Univ., Ottawa, ON, Canada, March 1995.

[8] Bergmans, J. L., "Tether Laboratory Demonstration System (TE-LAB); Payload Orientation Determination System, Rotation Rate Control, and Validation of Stability Criteria," M.S. Thesis, Mechanical and Aerospace Engineering Dept., Carleton Univ., Ottawa, ON, Canada, March 1995.

[9] Vigneron, F. R., Jablonski, A. M., and Chandrashaker, R., "Tether Dynamics Model For The Tether Laboratory Demonstration System (TE-LAB)," Canadian Space Agency, CSA TR OED-TR-93-05, St. Hubert, PQ, Canada, Nov. 1993.

[10] Vigneron, F. R., "A Natural Modes Model and Modal Identities for Damped Linear Structures," *Journal of Applied Mechanics*, Vol. 53, March 1986, pp. 33–38.

[11] Hughes, P. C., *Spacecraft Attitude Dynamics*, Wiley, New York, 1986, pp. 510–520.

[12] Eliuk, W., Walkty, I., Rob, R., Rumbold, G., and James, H. G., "OEDIPUS-C Tethered Suborbital Mission Description and Flight Performance," *Proceedings of the 9th CASI Conference on Astronautics*, Canadian Aeronautics and Space Inst., Ottawa, ON, Canada, 1996, pp. 332–341.